Acoustic planar surface retroreflector

Gang Yong Song,[1] Qiang Cheng,[1,*] Tie Jun Cui,[1,†] and Yun Jing[2,‡]

[1]*State Key Laboratory of Millimeter Waves, Department of Radio Engineering, Southeast University, Nanjing 210096, China*
[2]*Department of Mechanical and Aerospace Engineering, North Carolina State University, Raleigh, North Carolina 27695, USA*

This article reports on the design, numerical simulation, fabrication, and experimental test of an acoustic planar retroreflector capable of effectively reflecting sound along its incident direction for a wide operating angle range ($0°-70°$). The proposed acoustic planar retroreflector is a compound of two cascaded metasurfaces: a transmissive surface that converges the incident beam onto a second planar surface placed behind it, which serves as a reflective surface that bounces the beam back along the incident direction. Both the simulated and measured results provide evidence of the sound retroreflection effect. The structure proposed here provides a possible strategy for improving medical ultrasound, underwater communication, and illusion device design.

I. INTRODUCTION

Retroreflectors originated from the field of electromagnetic (EM) waves [1–7], and they are capable of generating radiation flux in a direction opposite and parallel to the incident direction. A reflector with this unique feature, however, has been largely unexplored in another extremely important wave physics field, i.e., acoustics. An acoustic retroreflector, similar to its EM wave counterpart, allows the maximum amount of reflected energy to return to the acoustic source/sensor, considerably enhancing the signal-to-noise ratio (SNR) of the received signal and facilitating a variety of applications such as remote sensing [8], nondestructive detection [9], medical ultrasound imaging [10], music performance monitoring [11], and underwater communication [12]. Conventionally, the acoustic retroreflector can be realized by three mutually perpendicular intersecting plates (corner retroreflector) [11,12]. Limited by the acoustical properties of natural materials, traditional methods for acoustic retroreflectors necessarily involve configurations of large size, curved shape, limited incident angles, and performance, thus hindering their applications in solving real-world problems.

There has been considerable focus on recent progress with acoustic metamaterials because they have extreme parameters unattainable with natural materials [13–24]. Notably, an acoustic metasurface, a type of acoustic metamaterial, has emerged as a versatile method for designing novel devices by virtue of rationally designed "two-dimensional" structures, and they have been demonstrated with many intriguing wave-shaping properties [25–29], such as self-bending beams [30], vortex beams [31], anomalous refraction/reflection [32], and diffuse reflection [33,34]. However, acoustic retroreflectors based on artificial materials/structures have been largely unexplored until recently, when a bulk acoustic retroreflector was proposed based on the mirrored Luneburg lens [35]. In this article, we explored whether it was possible to build a wide-angle, high-

efficiency acoustic retroreflector by leveraging the functionalities of acoustic metasurfaces with planar surface. We attempted to answer this question by designing and demonstrating an acoustic planar retroreflector (APR). Our proposed structure is a composite material that cascades two metasurfaces composed of transmissive and reflective elements that are designed independently but work synergistically to give rise to the desired effect of retroreflectance. The resulting device has an overall planar shape yet is capable of reflecting the sound beam along the incident direction. The retroreflection performance is demonstrated by manipulating sound waves in three-dimensional (3D) space both numerically and experimentally.

II. THEORY AND DESIGN

A. Conceptual design

Figures 1(a) and 1(b) show the conceptual design schematics for achieving acoustic retroreflection. Figure 1(a) displays the cross section of a conventional cat's-eye retroreflector comprising a focusing lens and a concave mirror, which behave like a cat's-eye device in optics [1–3]. Note that this type of retroreflector is a volumetric device that operates in 3D [1,2] space, while here we only show 2D images (the cross section) for simplicity in order to clarify the concept of the retroreflector. The ray of the incident beam with an angle of θ_i can be reflected back in the same direction because the concave mirror locally yields a surface that is oriented normal to the incident wave, and this effect is made possible by the focusing lens situated above the mirror. The strategy of combining two metasurfaces or planar surfaces (PS) to build an APR is illustrated in Fig. 1(b). The two PSs consist of an array of inhomogeneous elements on a flat substance. The element parameters are determined so that the APR is equivalent to the traditional cat's-eye retroreflector shown in Fig. 1(a). The incident radiation on the first PS was focused onto a local region on the second PS, which consists of reflecting units. The sound passes through the first PS again after the reflection. To have a working device, PS II needs to impart a spatially varying wave vector given by $\boldsymbol{k}_{\parallel}^r = \boldsymbol{k}_{\parallel}^i + \boldsymbol{k}^{\mathbf{retro}}$, under the condition that $\boldsymbol{k}^{\mathbf{retro}} = -2\boldsymbol{k}_{\parallel}^i$,

---
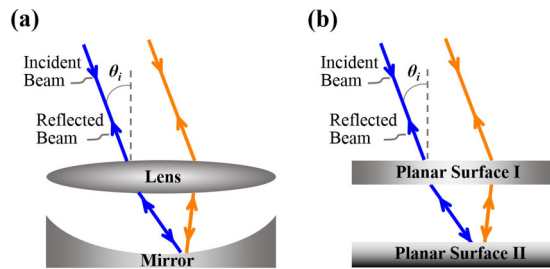*qiangcheng@seu.edu.cn
†tjcui@seu.edu.cn
‡yjing2@ncsu.edu

FIG. 1. (a) Schematic illustration of a cat's eye retroreflector composed of a focusing lens and a concave mirror. (b) Illustration of the proposed acoustic APR composed of two planar surfaces. Planar surface I directs waves with different incident angles to different spots on planar surface II. Planar surface II is a gradient surface and adds a spatially varying wave vector equal to twice that of the wave, but with the opposite sign.

where $k_{||}^r$, $k_{||}^i$, and $k^{\mathbf{retro}}$ are the in-plane wave vectors of the reflected beam, the incident beam, and the retroreflectively added wave vector, respectively [4]. After being refracted for the second time under the above condition of wave-vector flipping, the wave comes out of PS I in an approximate collimated beam strictly in the reverse direction. Moreover, the thickness of each PS of the proposed acoustic retroreflector is approximately 0.5λ, which is far thinner than the conventional device with a thickness close to 5λ or larger [2,12].

B. Unit cell design

To design the APR, we selected the space-coiling structure [32,36–38] as the transmissive element depicted in Fig. 2(a), and the vertical-cavity structure [39–42] sketched in Fig. 2(c) as the reflective element. The space-coiling structure is able to manipulate transmitted waves due to the fact that they can heavily delay the sound travels therein [32,36–38]. Using the design procedure shown in the supplemental material [43], we fine-tuned the beam length (h_{trans}) of the transmissive element to render a full 2π delay for the phase at the operating frequency of 6 kHz [Fig. 2(a)]. The required position-dependent phase shifts can be obtained from Eqs. (1) and (2), as shown below. The resulting phase and its corresponding transmittance are shown in Fig. 2(b) and they are retrieved via finite-element-method (FEM) simulations using COMSOL MULTIPHYSICS 5.2a [43]. Here, the transmittance/reflectance is defined as the ratio of the pressure amplitude between the transmitted/reflected wave and the incident wave. These ratios can be calculated from the simulated transmission and reflection spectra based on a standard transfer-matrix technique [44]. In Fig. 2(b), it is observed that the transmission amplitude and phase change sharply for certain values of h_{trans} (marked by the gray rectangle) due to the Fabry-Pérot (FP) resonance. However, this resonance is affected by the thermoviscous losses in the system [45–47], which, for simplicity, were not considered in our modeling. The corresponding h_{trans} of the gray rectangle area was not used in our design due to the abruptly changing phase. The geometrical parameters (t_1, m_1, p_1, w, s_1) can be found in the caption of Fig. 2(b).

Similarly, based on the aforementioned design method, the employed reflective PS II element, shown in Fig. 2(c),
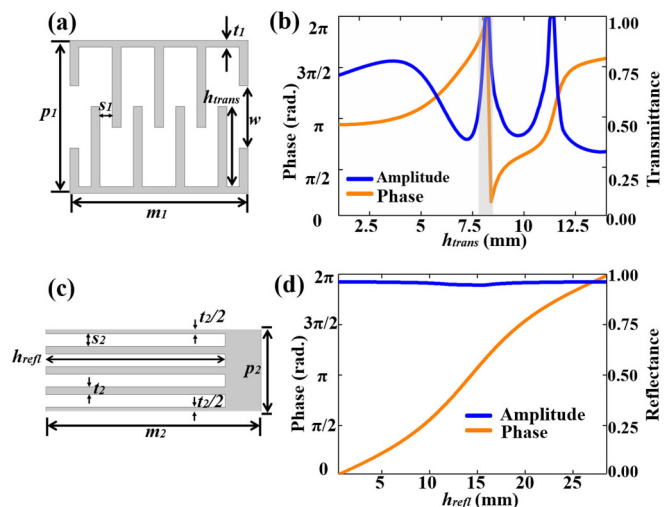

FIG. 2. (a) Schematic of the transmissive element used to implement PS I. The element was composed of a space-coiling structure. The space-coiling structure had a length $m_1 = 20$ mm, width $p_1 = 17.86$ mm, rigid wall thickness $t_1 = 1$ mm, inner air channel width $s_1 = (m_1 - 9t_1)/8$, and slit dimension $w = 9$ mm. h_{trans} could be adjusted to obtain a span of 2π phase shift. (b) Simulated transmittance and transmission phase as a function of h_{trans} of the inner wall. (c) The reflective element design for PS II. The element consisted of five rigid walls and background air in-between, and the parameter dimensions were as follows: length $m_2 = 30$ mm, width $p_2 = 8.57$ mm, rigid wall thickness $t_2 = 1$ mm, inner air channel width $s_2 = (p_2 - 4t_2)/4$. The height h_{refl} could be tuned to realize a 2π shift of the reflective phase. (d) Reflectance and reflection phase as a function of h_{refl}.

was composed of five rigid posts, four vertical cavities filled with air, and a hard backing wall to reflect the sound. Sound experiences two phase shifts induced by the reflective unit cells due to the round-trip that occurred in this structure. The reflected phase can be tuned from 0 to 2π at 6 kHz by adjusting the length of the cavity (h_{refl}). The reflectance and the reflection phase of the reflective element as a function of length h_{refl} are shown in Fig. 2(d), indicating that high reflectance is achieved by varying h_{refl} from 0.5 to 29 mm. We did not employ $h_{\text{refl}} = 14.16$ mm ($\lambda/4$ @ 6000 Hz) in the design because of the well-known $\lambda/4$ resonance, which could cause strong sound absorption in experiments [48]. The obtained average reflected ratio of the sound wave was as high as 98% in terms of the pressure amplitude, which is a crucial condition for achieving an efficient APR. Here, other structures that are potentially thinner can also be used for the reflective element here [37].

C. APR fabrication and working principle

The APR was finally constructed through the combination of PSs I and II as a series of concentric rings. The design procedures of PS I and II are illustrated in Figs. 3(a) and 3(b), where the transmissive and reflective unit cells are labeled with the numbers and rotated $360°$ about the z axis. The radii R_1 and R_2 are 250 and 300 mm, respectively. These dimensions were chosen merely for convenience. Note that a holder across the center of PS I serves to anchor the discrete structures shown in the subgraph of Fig. 3(a). Figure 3(c) illustrates the working principle of the APR. In our design, the materials for
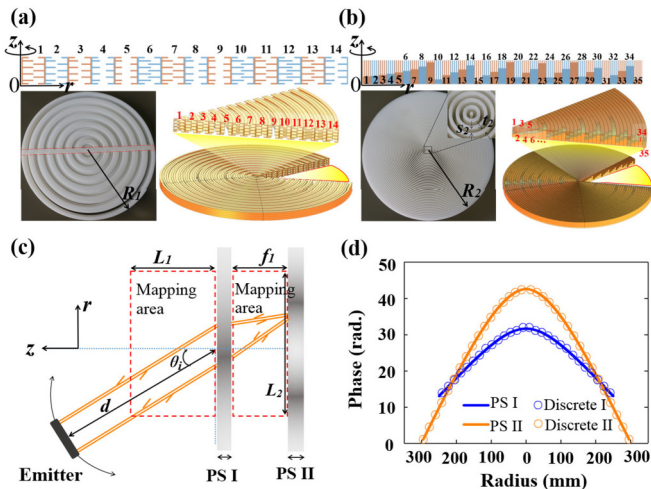
FIG. 3. (a) PS I photograph and its corresponding sketch. (b) PS II photograph and its corresponding sketch. (c) Schematics of the experimental setup. The rectangle defined by the dashed lines defines the areas $L_1 \times L_2$ and $f_1 \times L_2$ scanned by the receiver where $L_1 = 15$ cm, $L_2 = 30$ cm, and $f_1 = 10$ cm. (d) Phase profiles of PS I, PS II, and their discrete values. In this design, we initially created 14 elements (35 elements) for the transmissive (reflective) structure, and we arranged all the elements in radial directions with no gap between neighboring unit cells. Then, by rotating all the unit cells 360° about the vertical axis (z axis) at the origin ($r = 0$), PS I and II could be obtained as shown in Figs. 3(a) and 3(b), respectively.

composing the PS I and II were photosensitive resin and were assumed to be acoustically rigid. In our work, the wall of each unit cell was sufficiently thin (1 mm) compared to the thickness (i.e., p_1 and p_2) with the thickness ratio 0.06 and 0.12 for PS I and PS II respectively, where the thickness ratio is defined as the ratio between the wall thickness (t_1 or t_2) and the unit cell thickness (p_1 or p_2).

To understand how APR works, it is important to understand the design principles of PSs I and II. PS I serves as a planar lens with a focal length being the distance between the two PSs. Therefore, incident waves will be focused on the surface of PS II. Such a planar lens usually features a hyperbolic phase profile, with the maximum phase delay at the center due to the reduced path length for wave propagation. The phase distribution along the lens [Fig. 3(d)] can be written as [37,49]

$$\phi^{\mathrm{I}}(r) = \frac{2\pi}{\lambda_0}\left(\sqrt{f_1^2 + r^2} - f_1\right), \qquad (1)$$

where f_1 and λ_0 represent the focal length and the wavelength, respectively, and r is the radius of the planar lens.

In the case of the oblique incidence at angle θ_i, the ray traveling through the center of PS I will arrive at the position (x', y') of PS II without bending. To determine the phase distribution of PS II, we gradually increased the incident angle and examined the reflection phase at (x', y') via an iteration procedure. As an example, for one cross section of the APR [Fig. 3(c)], if the acoustic wave is incident toward a gradient metasurface at the angle of θ_i, the reflection angle θ_r is determined by both the incident angle and the surface phase

gradient [41],

$$(\sin\theta_r - \sin\theta_i)k_0 = \nabla\phi_s, \qquad (2)$$

where ϕ_s is the position-dependent phase modulation along PS II, and $k_0 = 2\pi/\lambda_0$ is the wave number of the background medium. To achieve retroreflection with $\theta_r = -\theta_i$ at the surface of PS II, the phase gradient at r'_n can be approximately obtained from Eq. (2)

$$\frac{\partial\phi^{\mathrm{II}}}{\partial r'} \approx \frac{\phi_n^{\mathrm{II}} - \phi_{n-1}^{\mathrm{II}}}{r'_n - r'_{n-1}} = -2k_0\sin\theta_i \quad (n = 1, 2, \ldots), \qquad (3)$$

where ϕ_{n-1}^{II} represents the phase at the neighboring point r'_{n-1}. The overall phase profile of PS II is shown as the orange line with circles in Fig. 3(d). The hyperbolic feature of the phase curve can be well understood as PS II, which should bounce back all the rays across the center of PS I, corresponding exactly to the requirement of a focusing lens (PS I). In our design, PS II was discretized into a number of concentric arrays of straight wells on a flat surface, as schematically illustrated in Fig. 3(b), where each set of 4-well serves as an individual element, satisfying the phase shift demand of PS II.

III. SIMULATION RESULTS

Numerical simulation of the retroreflector was initially performed using the setup shown in Fig. 3(c) and the acoustic-solid interaction module of COMSOL MULTIPHYSICS. Please note that thermoviscous losses were not considered here since the simulations were performed in 3D and the addition of the boundary layer made the simulation extremely challenging due to the large amount of compute memory and time needed to acquire accurate results. However, as can be seen below, we were still able to obtain good agreement between the simulation and measurement. The incident sound beam was modeled with a quasi-plane-wave beam radiating from a finite-size source with dimensions of 13 cm×1.5 cm, mimicking the dimensions of the speaker array used in the experiment. The simulation for beam retroreflectance was conducted by varying the incident angles, θ_i. Notice that the designed APR was circularly symmetric, and the axes of rotation for PSs I and II were identical.

Figure 4(a) demonstrates the total field intensity distribution when the acoustic beam propagated toward the retroreflector at a frequency of 6 kHz and the angle of incidence was 40° with respect to the normal direction of the sample. The standing-wave pattern was evident due to the interaction between the incident wave and reflection. For comparison, acoustic focusing can be clearly observed in the presence of PS I alone as shown in Fig. 4(c). Figure 4(d) shows the scattering field intensity to help explain the scattering behavior of the proposed structure, in which the contribution of the incident wave was removed in COMSOL. The scattered beam was directed mainly along the same angle of the incident beam, as expected. Interference patterns were also seen here, possibly due to the scattering off PS I. By comparing Figs. 4(a), 4(c), and 4(d), we observed that the proposed APR did produce the retroreflection effect where the incident sound wave was focused by PS I and was reflected back along the same direction by PS II. The overall simulated retroreflectance profiles are shown in Figs. 5(a)–5(h) for eight incident angles θ_i ranging from 0° to 70° with a step of 10°,
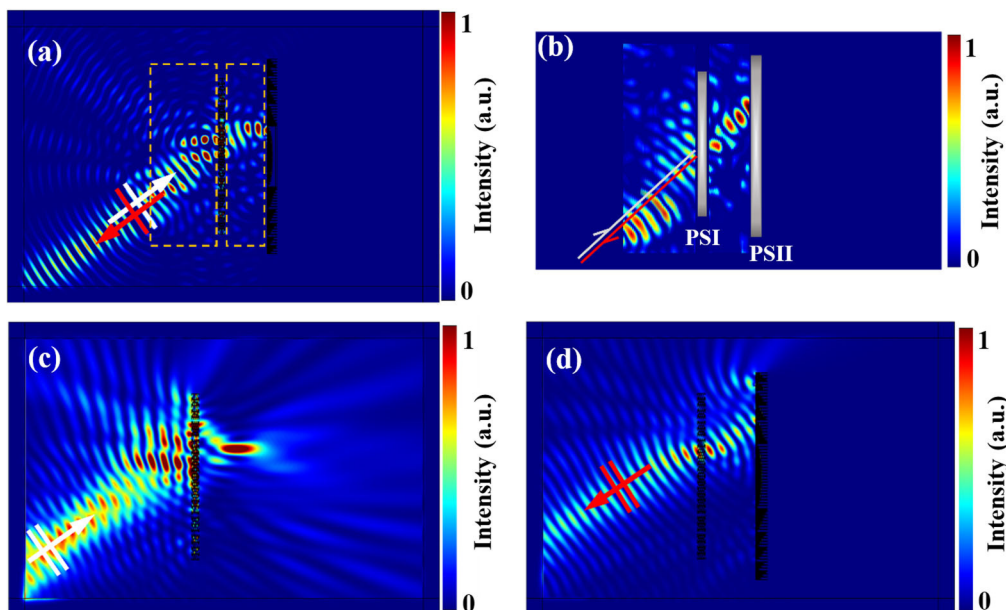
FIG. 4. (a) Simulated total field intensity for an impinging beam at a frequency of 6 kHz with a 40° angle of incidence, and (b) measured total field intensity in the rectangular areas enclosed by dashed lines shown in (a). (c) Simulated sound field without PS II shows the focused beam. (d) Simulation of the scattered sound field of the APR was performed by removing the incident wave component. The white and red lines with arrows denote the incident and reflected wave directions, respectively.

demonstrating the desired performance of the APR. From the simulation results in Fig. 5, it is clear that the reflected wave was mainly directed along the original direction (incidence direction) within the angular range from 0° to 70°, and there was no significant scattering observed in other directions. This strongly suggests that the proposed structure was able to reflect acoustic waves in the exact backward direction. It is worth noting that at many angles, high-order diffraction modes arose, due to the periodic nature of the elements, which may introduce an additional lattice vector to the surface phase gradient.

IV. EXPERIMENTAL RESULTS

Photographs of PS I and II samples are given in Figs. 3(a) and 3(b), respectively. The scheme of the experimental setup employed for the measurements was the same as that in the simulation shown in Fig. 3(c). The experiment was carried out in a three-dimensional open space, and the pressure fields were

recorded in the cut planes (i.e., mapping areas) in the vicinity of PS I and PS II, as shown in Fig. 3(c). Briefly, the APR was mounted on a rotary holder so that the angle of the incident beam could be adjusted. The incident beam traveled a center-to-center distance of $d = 25$ cm between the sound source and the front face of PS I. The emitted signal was a short chirp for which the energy was distributed around 6 kHz produced by a nine-speaker array, generating a quasi-plane-wave beam. A receiver-transducer of diameter 1/4 in. was moved to scan the sound pressure over the two rectangular areas of $L_1 \times L_2$ and $f_1 \times L_2$ with steps of 2 mm. The longer side (L_2) of this rectangle was parallel to the sample, and the dimensions can be found in the caption of Fig. 3(c). At each position, the receiver acquired the sound pressure, which was then processed through the Fourier transform to obtain the frequency-domain result. It is worth pointing out that the emitted signal was pulsed, and the reception was performed within a short window to avoid unwanted reflections from the surrounding environment.
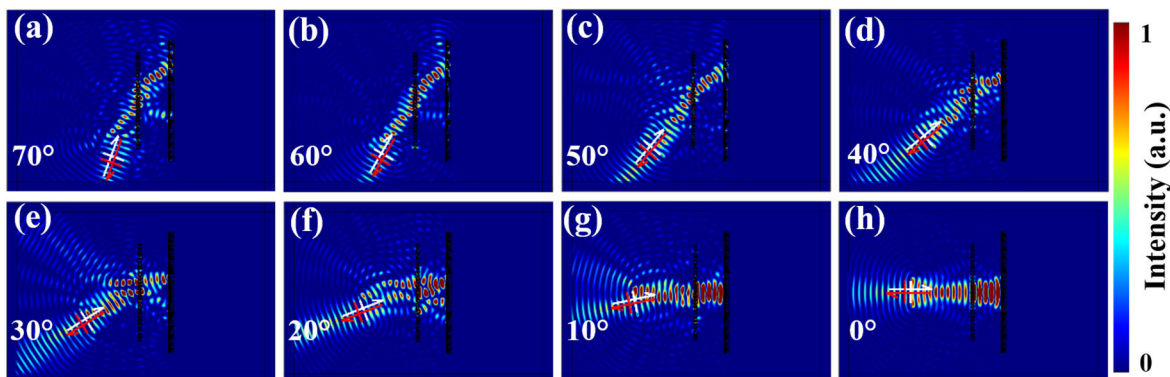

FIG. 5. (a)–(h) The simulated total sound field energy profiles of the APR as a function of incident angle ranging from 0° to 70° in 10° steps.
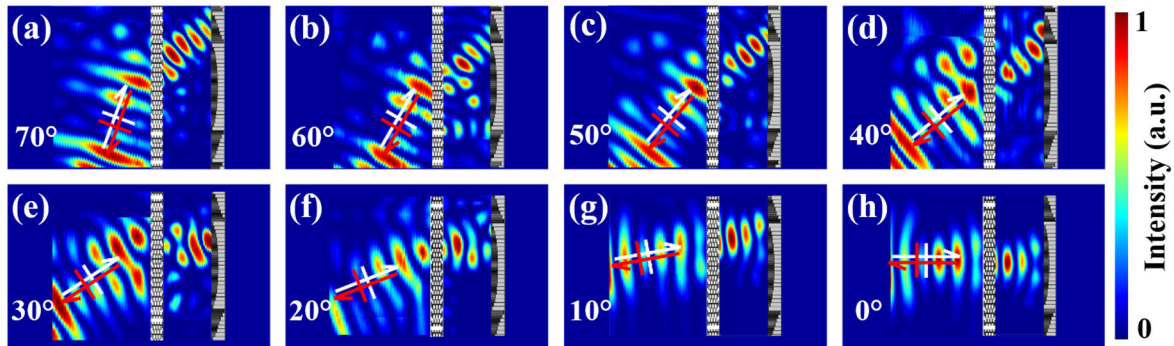
FIG. 6. (a)–(h) Measured total sound field energy for incident angles ranging from 0° to 70° in 10° steps.

Figure 4(b) exhibits a snapshot of the measured pressure map for the angle $\theta_i = 40°$ where the total sound field intensity containing the retroreflected beam energy was clearly observed. The measured data in Fig. 4(b) agree well with the simulated results of Fig. 4(a), both showing that APR can effectively bounce back the acoustic energy along its incident direction. The measured retrorefraction as a function of the incident angle is illustrated in Figs. 6(a)–6(h), which present the acoustic energy profiles in the mapping areas, where the white and red lines with arrows represent the incident and reflected wave directions, respectively. The sound beam aberration can be observed in Figs. 6(a)–6(h) as the incident angle changes from 0° to 70°. This effect is less severe in the simulation, as shown in Figs. 5(a)–5(h). There are a few possible reasons for the discrepancy between simulations and measurements. One comes from the inaccuracy of the sample manufacturing such as the roughness between the clamp holder and PS II. Another cause could be that the incident wave is not precisely captured by the simulation (e.g., due to unknown boundary conditions) so that the simulated wavefront is slightly different from that of the experiment. Finally, losses are not considered in simulations, which could also introduce deviations.

To quantitatively evaluate the retroreflectance of the APR, we used simulations and experiments to retrieve the retroreflection efficiency, which is defined as the energy ratio between the reflected and incident beams with $\eta = \frac{W_{\text{retro}}}{W_{\text{in}}}$, in which W_{retro} and W_{in} are the reflected and incident wave energy,
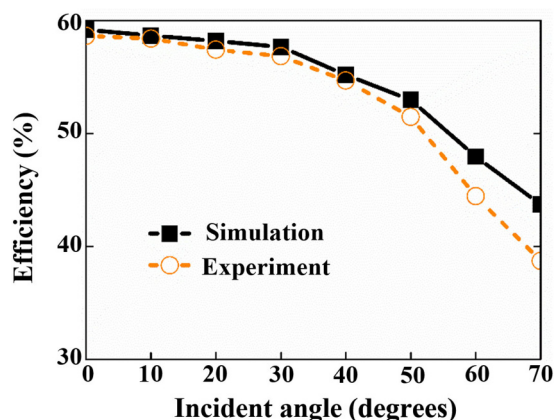
respectively. In the simulation, we retrieved the incident (p_{in}) and reflected (p_{retro}) acoustic pressure along a line (L, i.e., the white lines in Figs. 5 and 6) perpendicular to the propagation direction, and we integrated the pressure square field as $W_{\text{in}} = \frac{1}{\rho c_0} \int_L | p_{\text{in}}(\xi)|^2 d\xi$ and $W_{\text{retro}} = \frac{1}{\rho c_0} \int_L | p_{\text{retro}}(\xi)|^2 d\xi$, so that we could estimate the retroreflection efficiency. In the experiment, two rounds of measurements were conducted separately. We first measured the radiated wave from the speaker array in the absence of the sample in order to acquire the incident wave field. Then the sample was installed and we measured the total sound field, from which the scattering field could be obtained by subtracting the incident wave. Both the incident and scattering fields could be scanned along a line perpendicular to the propagation direction, so the retroreflection efficiency could be estimated similarly to the simulation. The reflection efficiency was measured and calculated as a function of the incident angle plotted in Fig. 7. The measured and simulated efficiency showed good agreement, both showing more than 50% efficiency for incident angles less than 50°. Figure 7 reveals that the measured efficiency was lower than that of the simulation, and both decreased as the incident angle increased. Nevertheless, the APR could still realize acoustic wave retroreflection in a wide range of angles (0°–70°), with acceptable efficiency (>40%).

V. CONCLUSIONS

In summary, we have designed, fabricated, and measured a flat retroreflector for airborne sound. The structure comprised two rationally designed metasurfaces, independently controlling the transmitted and reflected sound. The experimental results agreed well with the numerical simulations. The proposed scheme yielded relatively high efficiency as well as a wide range of working angles. The structure proposed in this work may pave the way for practical sound retroreflection devices, providing the possibility for realizing novel retroreflection functionalities that could be useful for applications such as ultrasound imaging and acoustic communication.

FIG. 7. The measured and simulated retroreflection efficiency as a function of incident angle.

[1] R. Beer and D. Marjaniemi, Appl. Opt. **5**, 1191 (1966).

[2] J. J. Snyder, Appl. Opt. **14**, 1825 (1975).

[3] S. Nemoto and J. Kida, Appl. Opt. **30**, 815 (1991).

[4] A. Arbabi, E. Arbabi, Y. Horie, S. M. Kamali, and A. Faraon, Nat. Photon. **11**, 415 (2017).

[5] Y. G. Ma, C. K. Ong, T. Tyc, and U. Leonhardt, Nat. Mater. **8**, 639 (2009).

[6] A. M. H. Wong, P. Christian, and G. V. Eleftheriades, in *Proceedings of the United States National Committee of URSI National Radio Science Meeting, Boulder* (IEEE, Piscataway, NJ, 2017).

[7] V. S. Asadchy, A. Díaz-Rubio, S. N. Tcvetkova, D. H. Kwon, A. Elsakka, M. Albooyeh, and S. A. Tretyakov, Phys. Rev. X, **7**, 031046 (2017).

[8] D. R. Dowling and K. G. Sabra, Annu. Rev. Fluid Mech. **47**, 221 (2015).

[9] Y. Solodov, Ultrasonics **36**, 383 (1998).

[10] J. Huang, P. Dupont, A. Undurti, J. Triedman, and R. Cleveland, Ultrasound Med. Biol. **32**, 721 (2006).

[11] H. T. Tuominen, J. Rämö, and V. Välimäki, in *Proceedings of the Sound and Music Computing Conference, Stockholm* (Zenodo, Genève, Switzerland, 2013).

[12] C. Prada, J. de Rosny, D. Clorennec, J. Minonzio, A. Aubry, M. Fink, L. Berniere, P. Billand, S. Hibral, and T. Folegot, J. Acoust. Soc. Am. **122**, 761 (2007).

[13] Z. Liu, X. Zhang, Y. Mao, Y. Y. Zhu, Z. Yang, C. T. Chan, and P. Sheng, Science **289**, 1734 (2000).

[14] N. Fang, D. Xi, J. Xu, M. Ambati, W. Srituravanich, C. Sun, and X. Zhang, Nat. Mater. **5**, 452 (2006).

[15] J. Zhu, J. Christensen, J. Jung, L. Martin-Moreno, X. Yin, L. Fok, X. Zhang, and F. J. Garcia-Vidal, Nat. Phys. **7**, 52 (2011).

[16] M. Yang, G. Ma, Y. Wu, Z. Yang, and P. Sheng, Phys. Rev. B **89**, 064309 (2014).

[17] X. Ao and C. T. Chan, Phys. Rev. B **80**, 235118 (2009).

[18] I. Spiousas, D. Torrent, and J. Sanchez-Dehesab, Appl. Phys. Lett. **98**, 244102 (2011).

[19] C. Shen, J. Xu, N. X. Fang, and Y. Jing, Phys. Rev. X **4**, 041033 (2014).

[20] Y. Ding, Z. Liu, C. Qiu, and J. Shi, Phys. Rev. Lett. **99**, 093904 (2007).

[21] T. Y. Huang, C. Shen, and Y. Jing, J. Acoust. Soc. Am. **139**, 3240 (2016).

[22] S. A. Cummer, J. Christensen, and A. Alu, Nat. Rev. Mater. **1**, 16001 (2016).

[23] G. Ma and P. Sheng, Sci. Adv. **2**, e1501595 (2016).

[24] Y. Xie, C. Shen, W. Wang, J. Li, D. Suo, B.-I. Popa, Y. Jing, and S. A. Cummer, Sci. Rep. **6**, 35437 (2016).

[25] J. Zhao, B. Li, Z. N. Chen, and C. W. Qiu, Appl. Phys. Lett. **103**, 151604 (2013).

[26] Y. Xie, W. Wang, H. Chen, A. Konneker, B. I. Popa, and S. A. Cummer, Nat. Commun. **5**, 5553 (2014).

[27] Y. Li, G. K. Yu, B. Liang, X. Y. Zou, G. Y. Li, S. Cheng, and J. C. Cheng, Sci. Rep. **4**, 6830 (2014).

[28] Y. Cheng, C. Zhou, B. G. Yuan, D. J. Wu, Q. Wei, and X. J. Liu, Nat. Mater. **14**, 1013 (2015).

[29] Y. Li, C. Shen, Y. Xie, J. Li, W. Wang, S. A. Cummer, and Y. Jing, Phys. Rev. Lett. **119**, 035501 (2017).

[30] Y. Li, X. Jiang, B. Liang, J.-c. Cheng, and L. Zhang, Phys. Rev. Appl. **4**, 024003 (2015).

[31] X. Jiang, Y. Li, B. Liang, J.-c. Cheng, and L. Zhang, Phys. Rev. Lett. **117**, 034301 (2016).

[32] K. Tang, C. Qiu, M. Ke, J. Lu, Y. Ye, and Z. Liu, Sci. Rep. **4**, 6517 (2014).

[33] Y. Zhu, X. Fan, B. Liang, J. Cheng, and Y. Jing, Phys. Rev. X **7**, 021034 (2017).

[34] N. Jiménez, T. J. Cox, V. Romero-García, and J. Groby, Sci. Rep. **7**, 5389 (2017).

[35] Y. Fu, J. Li, Y. Xie, C. Shen, Y. Xu, H. Chen, and S. A. Cummer, arXiv:1801.06775.

[36] Z. Liang and J. Li, Phys. Rev. Lett. **108**, 114301 (2012).

[37] Y. Li, B. Liang, Z. M. Gu, X. Y. Zou, and J. C. Cheng, Sci. Rep. **3**, 2546 (2013).

[38] T. Frenzel, J. D. Brehm, T. Bückmann, R. Schittny, M. Kadic, and M. Wegener, Appl. Phys. Lett. **103**, 061907 (2013).

[39] S. Zhai, H. Chen, C. Ding, F. Shen, C. Luo, and X. Zhao, Appl. Phys. A **120**, 1283 (2015).

[40] C. Faure, O. Richoux, S. Félix, and V. Pagneux, Appl. Phys. Lett. **108**, 064103 (2016).

[41] B. Liu, W. Zhao, and Y. Jiang, Sci. Rep. **6**, 38314 (2016).

[42] X. D. Fan, Y. F. Zhu, B. Liang, J. Yang, L. L. Yin, J. Yang, and J. C. Cheng, Appl. Phys. Lett. **109**, 153501 (2016).

[43] See Supplemental Material at http://link.aps.org/supplemental/10.1103/PhysRevMaterials.2.065201 for the design details on the unit cells and the retrieval method of phase and transmittance/reflectance based on simulation.

[44] ASTM-Standard Test Method for Measurement of Normal Incidence Sound Transmission of Acoustical Materials Based on the Transfer Matrix Method. 2009: ASTM.

[45] X. Jiang, Y. Li, and L. Zhang, J. Acoust. Soc. Am. **141**, EL363 (2017).

[46] V. C. Henríquez, V. M. García-Chocano, and J. Sánchez-Dehesa, Phys. Rev. Appl. **8**, 014029 (2017).

[47] G. P. Ward, R. K. Lovelock, A. R. J. Murray, A. P. Hibbins, J. R. Sambles, and J. D. Smith, Phys. Rev. Lett. **115**, 044302 (2015).

[48] X. Jiang, B. Liang, R. Q. Li, X. Y. Zou, L. L. Yin, and J. C. Cheng, Appl. Phys. Lett. **105**, 243505 (2014).

[49] S. Vo, D. Fattal, W. V. Sorin, Z. Peng, T. Tran, M. Fiorentino, and R. G. Beausoleil, IEEE Photon. Technol. Lett. **26**, 1375 (2014).